Journal of Materials Chemistry B

ROYAL SOCIETY OF CHEMISTRY

PAPER

View Article Online
View Journal | View Issue



Cite this: J. Mater. Chem. B, 2025, 13, 2029

# Nitrogen doped carbon dots for *in vitro* intracellular redox modulation *via* optical stimulation†

P. Lagonegro,‡*[ab] C. Marzuoli,‡[bc] G. Tullii,[b] F. Rossi,[d] C. Bellacanzone,[b] E. Mancinelli,[b] F. Turco,[a] B. M. Squeo,[a] M. Pasini*[a] and M. R. Antognazza[b]

Received 31st July 2024,
Accepted 23rd December 2024

DOI: 10.1039/d4tb01698j

rsc.li/materials-b

Carbon dots (CDs) are promising candidates as oxygen photosensitizers, in cancer therapeutic applications due to their high quantum yield, superior chemical and photostability, low cytotoxicity and ease of chemical functionalization/tuning. Nitrogen doping can further improve oxygen photosensitization performance. Besides photodynamic therapy, however, the possibility to finely and remotely regulate the intracellular redox balance by using physical stimuli has been attracting more and more interest not only for nanotheranostic application, but also as a novel, fully biocompatible therapeutic tool. Here, we report on the synthesis of nitrogen-doped CDs by solvothermal methods starting from abundant, bioderived, low-cost precursors, and we characterize their interface with *in vitro* cultures of human embryonic kidney (HEK-293) cells, a widely accepted model of non-tumoral cells. While not affecting cell proliferation, synthesized CDs efficiently modulate, under visible light and physiological *eu*stress conditions, intracellular calcium ion dynamics and reactive oxygen species concentration, resulting in a 4-fold increase. The reported results may broaden the application of CDs beyond photodynamic therapy, unveiling new opportunities in the field of redox medicine assisted by carbon-based nanomaterials and optical stimulation.



## Introduction

Carbon dots (CDs) represent one of the most recent additions to the carbon-based nanomaterial family. Discovered in the early 2000s,[1] these nanoparticles exhibit a spherical morphology with diameters below 10 nm.[2] They can be synthesized using both top-down approaches, such as the exfoliation of graphite, and bottom-up methods from carbon-rich precursors,[3] including plastic waste[4] or agro-industrial residues.[5] The carbon within these dots can exist in various hybridization states, ranging from fully amorphous[6] to having a graphitic core,[7,8] depending on the synthesis conditions.[9] This structural and compositional versatility endows carbon dots with a wide array of properties, making them a key subject of study in current nanotechnology research.[10] Among other applications, CDs have been largely employed for photocatalysis,[11] as sensitizers for solar cells[12] as well as for light emission and sensing,[1,13–15] taking full advantage of distinctive light absorption and charge generation capability. Nitrogen-doped carbon dots have also been reported, in combination with silver nanoparticles, as effective electrocatalysts for the oxygen reduction reaction, with high catalytic activity and superior stability compared to commercial Pt/C catalysts.[16] The peculiar properties of CDs have been exploited not only in the photonics and optoelectronic fields, but also in biotechnology.[17–19] Their excellent biocompatibility and water solubility are key features for their biological applications, in particular for *in vitro* cell labelling[20,21] and *in vivo* tissue imaging.[22] Bright photoluminescence in the visible spectrum, high photostability, broad excitation spectrum and tunable emission spectra promoted the use of CDs as a valuable alternative to conventional organic dyes and semiconductor quantum dots.[23] Thus, they have been explored as efficient light emitters for a range of techniques, including fluorescence imaging, magnetic resonance imaging, and photoacoustic imaging. Moreover, CDs have been explored as catalyst carriers in drug delivery systems, as well as active agents in photothermal and photodynamic tumor therapies.[24]

Nitrogen doping[25–30] is widely reported as an effective and sustainable method for modulating the optical properties of CDs (N-CDs).[31] By incorporating nitrogen in various forms such

[a] Istituto di Scienze e Tecnologie Chimiche "Giulio Natta" (SCITEC)-CNR, 20133 Milano, Italy. E-mail: mariacecilia.pasini@cnr.scitec.it
[b] Center for Nano Science and Technology, Istituto Italiano di Tecnologia, 20134 Milano, Italy. E-mail: paola.lagonegro@iit.it
[c] Dipartimento di Fisica, Politecnico di Milano, 20133 Milano, Italy
[d] IMEM-CNR Institute, Parco Area delle Scienze 37/A, 43124, Parma, Italy

† Electronic supplementary information (ESI) available. See DOI: https://doi.org/10.1039/d4tb01698j

‡ P. Lagonegro and C. Marzuoli equally contributed to this work.

as pyridinic, pyrrolic, or graphitic,[26] it is possible to tailor the electronic structure of N-CDs, leading to significant enhancements in their fluorescence and quantum yield. This flexibility allows for optimized light absorption and emission characteristics, which are crucial for different kinds of applications such as organic optoelectronics, smart packaging, photodynamic therapy and biosensing.[32–34]

Furthermore, nitrogen doping not only enhances the performance of CDs but also contributes to sustainability efforts, when urea, a biodegradable and widely available nitrogen source, is used for doping.[35] For instance, studies have shown that pyridinic-N enhances the electron density, facilitating better charge transfer processes and improving interactions with reactive oxygen species (ROS),[34,35] while pyrrolic-N-rich CDs are reported to show a downshift in the NIR absorption window with improved photothermal conversion.[30] The presence of graphitic nitrogen is reported to introduce mid-gap states within the energy bandgap of undoped carbon systems, which leads to a noticeable shift towards longer wavelengths in light absorption. This red-shifted absorption subsequently results in fluorescence emission at the lower-energy end of the visible spectrum.[27]

Relevant to the current work, it has been reported that copper and nitrogen co-doped CDs function as sensitizers for photodynamic therapy, effectively generating reactive oxygen species (ROS) under near-infrared (NIR) irradiation in mouse melanoma cells.[36] Interestingly, Wu *et al.* demonstrated that nitrogen doping improves oxygen photosensitization performance and correlated the observed changes in graphitic N and pyrrolic N with triplet activation and oxygen adsorption, which are the two main factors leading to oxygen photosensitization.[34] Overall, the photocatalytic properties of CDs, along with their ability to reduce oxygen and generate ROS, have been largely exploited for nanotheranostics applications.

Conversely, photoelectrochemically active CDs have never been considered, to the best of our knowledge, for their potential in modulating ROS levels under *eu*stress conditions,[37] *i.e.*, without adversely affecting cell viability and normal physiological function.

An increasing number of studies have shown that ROS, especially hydrogen peroxide,[38,39] are crucial mediators in maintaining the intracellular redox balance, which refers to the equilibrium between oxidizing and reducing agents within the cell cytosol. This dynamic equilibrium is essential for the proper physiological functioning of cells.[40] In fact, redox signaling tightly regulates several redox-sensitive biological pathways, including, among others, cell proliferation, growth and differentiation.[41] Thus, redox homeostasis is nowadays recognized as a core concept in cell physiology, leading to an increasing demand for novel functional materials capable of finely modulating intracellular ROS concentration at non-toxic levels. Several photoelectrochemically active, carbon-based materials, able to modulate intracellular ROS, have been recently reported by our and other groups.[42–46] A few promising examples include carbon nanotubes and graphene;[47–50] however, the large majority of efforts focused on conjugated polymers, mainly thiophene-based materials.[51–53]

Here, we propose the use of CDs, which may offer distinctive advantages as compared to other carbon-based materials, owing to their nano-dimensionality and superior capability to cross the cell membrane, easily tunable optical and electrical properties, and safe-by-design synthesis. We synthesize nitrogen-doped CDs by solvothermal methods starting from abundant, bioderived, low-cost precursors, and we characterize their optical and electrochemical properties both in an aqueous electrolyte at neutral pH and within *in vitro* cell cultures of human embryonic kidney (HEK-293) cells, a widely accepted model of non-tumoral cells. Experimental findings show that synthesized CDs do not adversely affect cell proliferation. Importantly, under visible light, they modulate intracellular calcium ion dynamics and affect the redox balance under physiological *eu*stress conditions, resulting in a 4-fold increase in intracellular ROS concentration.

These results extend the application of the photoelectrochemical properties of CDs beyond photodynamic therapy, unveiling new opportunities in the field of redox medicine assisted by carbon-based nanomaterials.

## Results and discussion

### 1. Synthesis and characterization

Nitrogen-doped CDs (N-CDs) were synthesized by making use of sustainable synthesis methods. While the role of nitrogen doping in tuning absorption and fluorescence optical properties has been largely reported,[54] its association with oxygen photosensitization, a potential key to optically modulate the intracellular ROS balance, has only recently been reported, by using as starting materials citric acid and ethylenediamine.[34] Here, CDs were synthesized starting from citric acid (CA), an abundant, cheap and non-toxic material, as the carbon source, and urea, as the nitrogen source, by solvothermal synthesis in dimethylformamide, as previously reported in the literature.[55–58] The purification step was then carried out by column chromatography. N-CD synthesis (see the Materials and methods section for all technical details) is schematically represented in Fig. 1(a). CD morphology and crystallinity have been determined by transmission electron microscopy (TEM) (Fig. 1(b)–(f)). Fig. 1(b) shows a representative bright field overview of the spherical shaped N-CDs distributed over the amorphous carbon support film of the TEM grid. Statistical analysis of the particle diameter gives a narrow size distribution centered at 3.25 nm. Atomic resolution TEM imaging proved that almost all the dots are crystalline. Fig. 1 shows the high-resolution TEM images (HRTEM, panels d–f) and the corresponding fast Fourier transforms (FFTs, panels g–i) of three selected dots, where the different sets of lattice planes with a spacing of 0.18 and 0.20 nm are clearly visible. The measured values of the lattice spacings and interplanar angles match those of graphite, imaged in different zone axes (*i.e.* ⟨211⟩ for the dot in Fig. 1(d), ⟨311⟩ for the dot shown in Fig. 1(e) and ⟨421⟩ for the dot in Fig. 1(f)). These results are in line with similar N-doped CDs obtained using biomass as a precursor *via* a hydrothermal technique.[59,60]

Fig. 2(a) shows optical absorption of CDs in water. A broad optical absorption signal is observed in the visible spectral

 

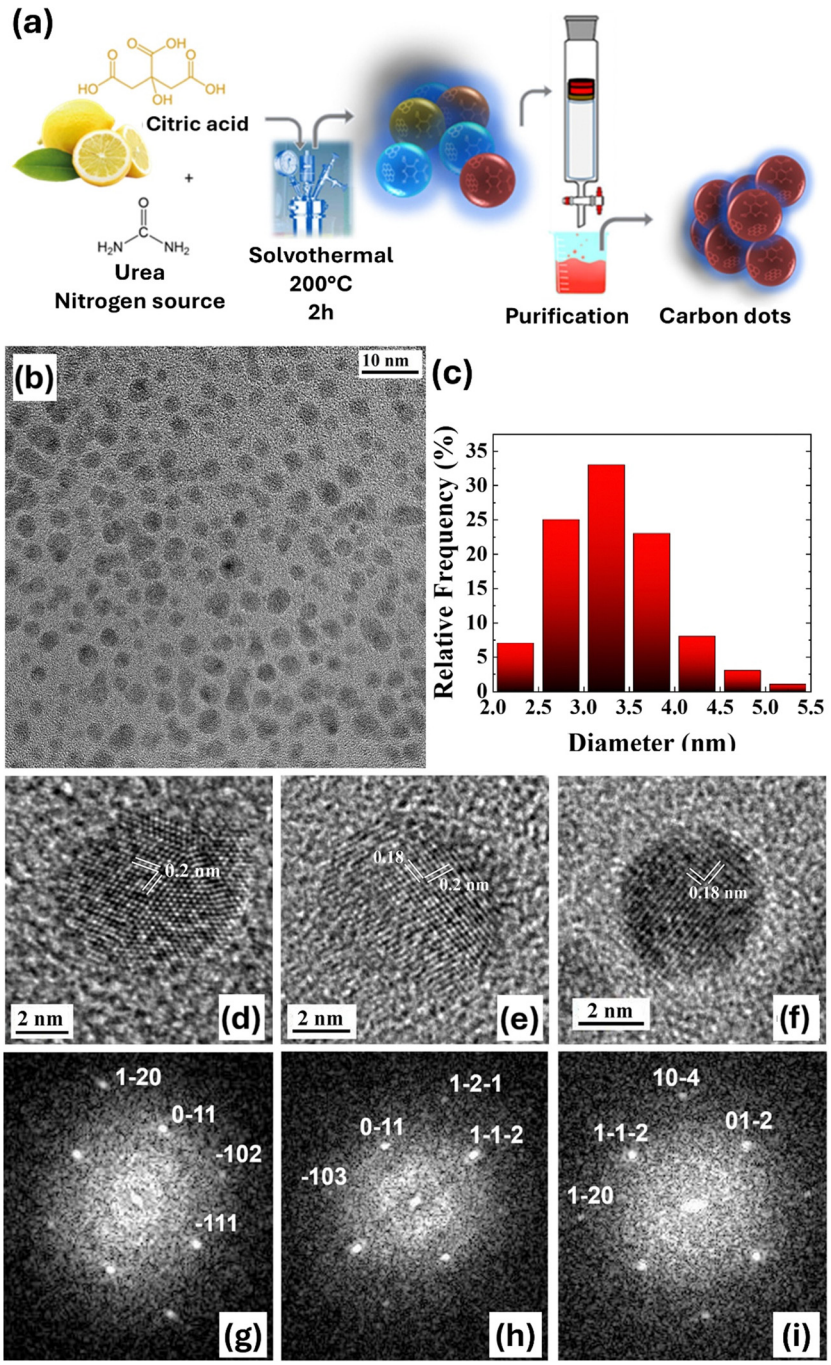


Fig. 1 (a) Schematic representation of the CD synthesis strategy, *via* solvothermal synthesis in water, followed by column chromatography for purification. (b) CD structural TEM analysis. Bright field overview image and (c) corresponding size distribution. (d)–(f) High resolution images of three representative single particles. (g)–(i) Fast Fourier transform (FFT) spectrum of the dots selected above in panels (d)–(f), respectively.

region, within the range of 300–600 nm. In more detail, the signal at low energy confirms the occurrence of the carbonization process, involving condensation, polymerization, carbonization, passivation and cross-linking steps, and leading to the formation of extended conjugation. Fig. 2(b) shows the Fourier transform infrared (FT-IR) spectrum of N-CDs. The presence of various functional groups containing C, N and O is confirmed. The stretching vibration spectral signatures of OH (3436 $cm^{-1}$), NH (3190 $cm^{-1}$), CH (2934 $cm^{-1}$), C=C (1617 $cm^{-1}$), C=N (1662 $cm^{-1}$), C=O (1727 $cm^{-1}$) and the bending vibrations between 1500 and 900 $cm^{-1}$ due to CH, CC, CN and CO, confirm the presence of conjugated aromatic structures together with O- and N-containing groups.[61]

X-ray photoelectron spectroscopy (XPS) analysis has been performed to quantify the nitrogen doping level and identify the specific nitrogen species present. Full-scan XPS spectra of

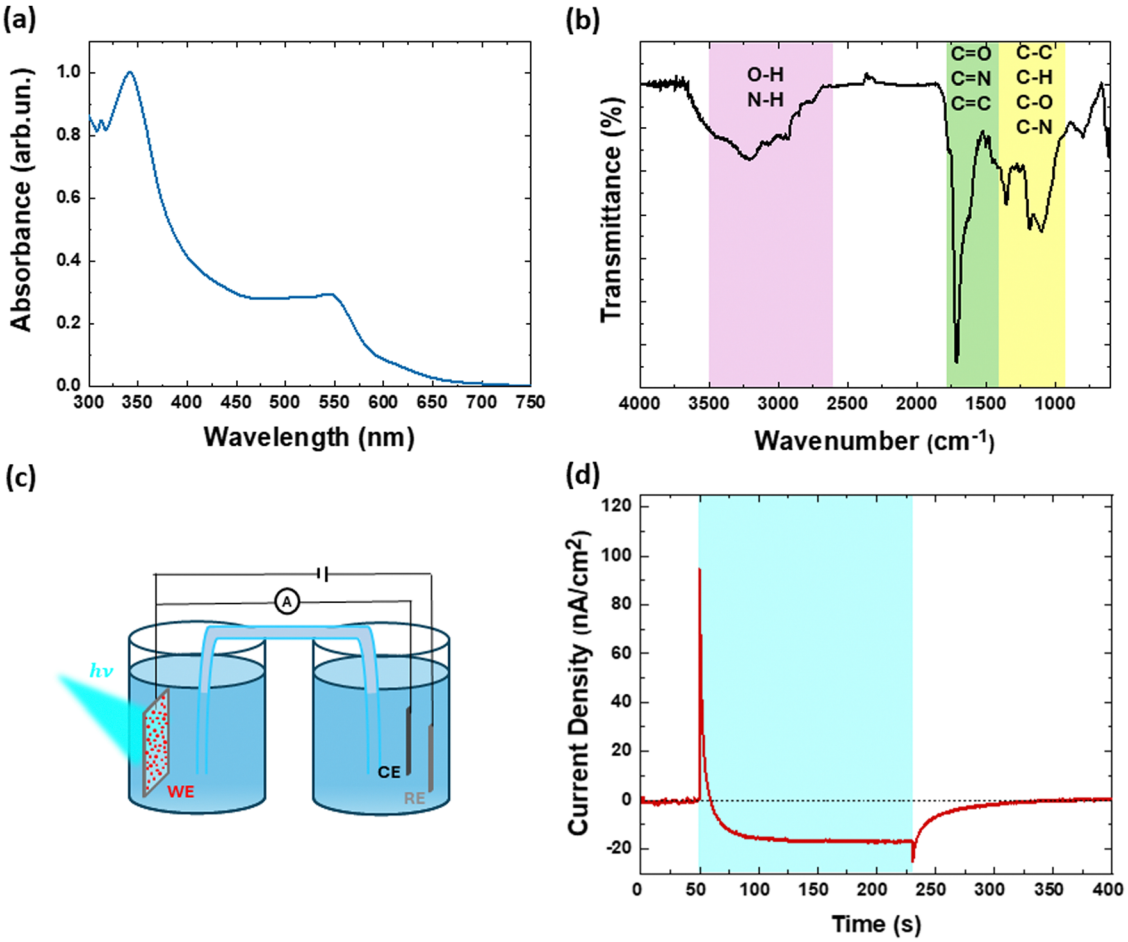


Fig. 2 (a) Normalized UV-vis absorbance spectrum. (b) FTIR spectrum of CDs shows the presence of various functional groups containing C and N, and O. (c) Sketch representing the experimental set-up employed for potentiostatic chronoamperometry measurements, consisting in an electrochemical cell in three electrode configuration, divided into two compartments, where a CD-treated ITO slab served as working electrode (WE) and a platinum wire and a Ag/AgCl electrode operated as the counter (CE) and reference (RE) electrodes, respectively. (d) Potentiostatic chronoamperometry data, as recorded in CDs drop cast onto ITO electrode. The cyan shaded area represents the illumination, impinging from the ITO side and lasting continuously for 3 minutes at 470 nm, 1.8 mW mm$^{-2}$ power density. The measurement is carried out at the OCP value, 160 mV *vs.* Ag/AgCl.

CDs (Fig. S1, ESI†) revealed three main peaks of interest at ~288.8 eV, ~399.5 eV, and ~531.5 eV, which correspond to C 1s, N 1s, and O 1s, respectively. Quantification of the full-scan XPS indicates that N-CDs contain 76% carbon, 11% nitrogen, and 11.8% oxygen. The high-resolution C 1s XPS spectrum was deconvoluted into five components based on different carbon species: sp$^2$ carbons (284.8 eV, main peak), sp$^3$ carbons (+1.0 eV), C–N and/or C–O bonds (286.9 eV), C═O bonds (288.3 eV), and COOR bonds (289.8 eV). The O 1s spectrum shows two main contributions consistent with the C 1s peaks: O–C bonds at 533.6 eV and O═C bonds at 531.2 eV. The N 1s lineshape was deconvoluted into three main nitrogen species: pyridinic N at 398.3 eV, pyrrolic N at 399.7 eV, and graphitic N at 400.8 eV. The results indicate that N-CDs contain 61.5% pyrrolic nitrogen, 18.9% pyridinic nitrogen, and 19.6% graphitic nitrogen (see the ESI,† Fig. S2 and Table S1). These nitrogen species significantly contribute to the photophysical properties of the N-CDs. Specifically, N-doped CDs exhibit red-shifted absorption and emission bands compared to non-doped CDs, as extensively reported in the literature.[25–27,62] Additionally, nitrogen doping plays a crucial role in modulating ROS.[63,64] Pyrrolic and pyridinic nitrogen, in particular, enhance $O_2$ adsorption and facilitate electron and energy transfer on the CD surface.[34,65–67] Moreover, graphitic nitrogen can reduce the energy gap between singlet and triplet states, promoting efficient inter-system crossing (ISC) and increasing the triplet state $T_1$ population, which enhances photosensitization efficiency.[34] The $^1$H NMR spectrum reported in Fig. S3 (ESI†) confirms the presence of heteroatoms, as indicated by hydrogen signals with chemical shifts typical of H–C, H–O, and H–N bonds of various types. In more detail, the spectrum shows a region corresponding to aliphatic protons, between 0 and 2.5 ppm; a region for non-aromatic protons bonded to heteroatoms between 5 and 6.5 ppm, and a region beyond 7 ppm attributed to aromatic protons, also bonded to heteroatoms, in agreement with the literature.[34,68]

Fig. 2(c) and (d) report, respectively, the photoelectrochemical set-up in 3-electrode configuration and a representative example of a chronoamperometry measured on CDs deposited

 

on indium tin oxide (ITO) electrode, in a standard physiological buffer (KRH) at neutral pH. The measurement was carried out at the electrochemical equilibrium, by applying constant bias equal to the open circuit potential value (preliminarily estimated in about 160 mV *vs.* Ag/AgCl), thus closely resembling the situation occurring within *in vitro* cell cultures. The cyan shaded area represents the illumination period (LED maximum emission wavelength, 470 nm; impinging on the sample from the ITO side, lasting continuously for 3 minutes, 1.8 mW $mm^{-2}$ power density). The dark current value is negligible, both before illumination onset and after illumination offset, with a fast recovery to the equilibrium situation. Upon illumination, a fast, positive photocurrent signal (build-up and decay time $<100$ ms, not resolved here) is observed, attributed to photocapacitive charging of the CDs/electrolyte interface, followed by a stable, long-lasting, negative photocurrent signal, assigned to a photofaradaic signal in a photocathodic configuration. Considering the typical timescales of biological pathways involved in metabolic processes ($>1$ s), we focus our attention to the faradaic regime. Based on previous works reporting chronoamperometry measurements in aqueous dispersion of carbon-based nanomaterials,[51–53] we attribute the photocathodic current to the occurrence of oxygen reduction reactions. In more detail, we hypothesize that upon visible light excitation CDs generate free charges, with holes recombining at the ITO interface and electrons being available for photoelectrochemical reactions at the aqueous interface (reaction (i)). Reduction of molecular oxygen dissolved in water produces metastable ROS, like, among other possibilities, superoxide ($O_2^-$) (reaction (ii)).

$$CDs + h\nu \rightarrow CDs^+ + e^- \quad \text{(i)}$$

$$e^- + O_2 \rightarrow O_2^- \quad \text{(ii)}$$

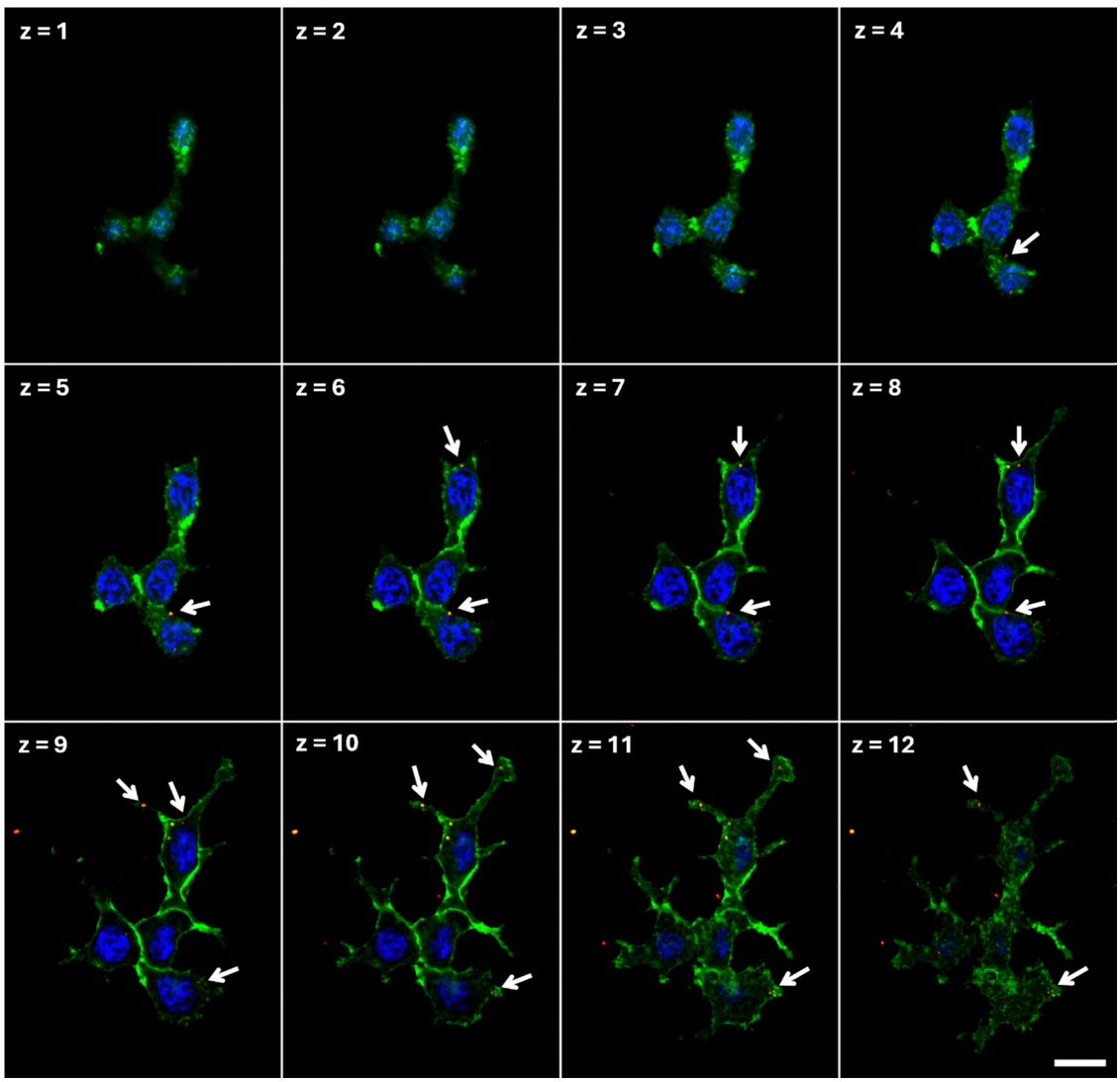


Fig. 3 Representative confocal images of HEK cells treated with CDs (25 μg $ml^{-1}$) acquired at different *z*-planes. Cells are stained with Cell Mask (cell membrane, green) and Hoechst 33342 (cell nuclei, blue). CDs can be visualized thanks to their emission spectral component at lower energy ($\lambda >$ 600 nm), thus avoiding any spectral overlap with nuclei and cell membrane markers, by proper use of dichroic mirror/emission filter combination. White arrows indicate the presence of CD aggregates. Images were acquired from top ($z = 1$) to bottom ($z = 12$). Interplane distance = 0.15 μm. Scale bar: 10 μm.

At equilibrium, ROS ends up in the formation of stable hydrogen peroxide ($H_2O_2$).

Several previous works described CDs as efficient ROS generators, and are in line with this picture.[69] The mechanism of $O_2^-$ generation in CDs is still not completely clarified and should be confirmed by a quantitative description of their energetic levels, by taking into account the energetic broadening due to the interaction with the aqueous buffer.[70] Overall, however, the observed photocathodic current indicates the occurrence of photoelectrochemical reactions, and corroborates the possibility to use N-CDs as biocompatible ROS generators for optically driven, drug-free modulation of the intracellular redox balance.

## 2. *In vitro* biohybrid interfaces between N-CDs and human embryonic kidney (HEK-293) cells

To evaluate the potential use of N-CDs for photomodulation of intracellular ROS, we investigate the interaction between CDs and HEK-293 cells, a widely recognized cell model for the study of nano-biohybrid systems. First, we employ confocal microscopy to assess the ability of CDs to stably internalize within the cell cytosol (Fig. 3). CDs can be visualized by taking advantage of their intrinsic photoluminescence properties (Fig. S4, ESI†); representative confocal images acquired in untreated samples are reported in Fig. S5 (ESI†) to the sake of qualitative comparison with CD-treated cell cultures. After CD treatment (20 hours) and subsequent rinses with fresh medium, confocal images are acquired at different $z$-planes, from the top surface ($z = 1$) of the cell to the bottom cell–substrate interface ($z = 12$). Confocal resolution only allows for discriminating CD aggregates, which clearly cross the cell membrane (green in Fig. 3) and distribute in a perinuclear region, but do not cross the nuclear membrane (nuclei, blue in Fig. 3). Penetration of single CDs into the cell nucleus cannot be excluded at this stage and should be addressed by in-depth super-resolution imaging, which is beyond the goal of the present work.

The impact of three different concentrations of CDs on HEK-293 viability is evaluated by the AlamarBlue metabolic assay (Fig. 4(a)). Three hours after plating HEK cells on glass substrates, CDs are added to the cell cultures at different concentrations (5, 10, 25 μg ml$^{-1}$). Alamar Blue fluorescence intensity is proportional to the metabolic activity of the cells, providing a direct indication of their proliferative capability. Data have been acquired at 24, 48 and 168 hours after plating. At each time point, and for all CD concentrations, no statistically significant difference is observed between CD-treated cells (dark red histograms in Fig. 4(a)) and untreated control cell cultures (black histograms in Fig. 4(a)). This indicates that the presence of CDs does not negatively affect cell proliferation. Additional cell viability tests were also carried out by employing a colorimetric assay based on MTT (Fig. S6, ESI†). In this case we considered two different time points, 1 and 5 days *in vitro* (DIV) after seeding, and three different CD concentrations (10, 50 and 200 μg ml$^{-1}$). At the highest concentration value, at DIV5, we observe a statistically significant decrease in cell viability (Fig. S6b, ESI†); conversely, CDs doses up to 50 μg ml$^{-1}$ do not show sizable impact on cell metabolism and proliferation capability, thus confirming the results obtained with the Alamar Blue assay.

Since the target of the present work is to exploit the photocatalytic properties of CDs towards oxygen reduction, it is important to assess their cytocompatibility upon photoexcitation (Fig. 4(b)). Based on the literature data for different cell types, including human adipose stem cells[71] and endothelial cells,[72] we employ a chronic light illumination protocol that did not show detrimental effect on cell growth and proliferation. We illuminate HEK-293 cell cultures, maintained at 37 °C and 5% $CO_2$, using an LED with an emission peak centered at 470 nm. This wavelength corresponds to the lower energy tail of the CD absorption spectrum, intentionally avoiding the maximum absorbance in the UV-blue region. Cells are exposed to continuous illumination for 6 hours, using a pulsed protocol

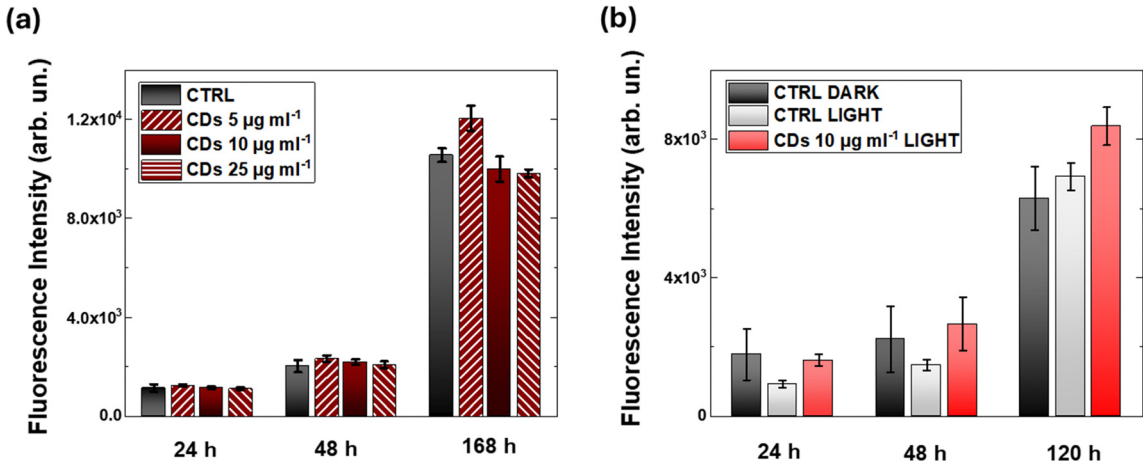


Fig. 4 (a) AlamarBlue cell proliferation assay in the dark: 3 CD concentrations (5, 10, 25 μg ml$^{-1}$) were considered and evaluated 24, 48, 168 hours after plating. (b) AlamarBlue cell proliferation assay upon photoexcitation (470 nm LED emission peak, 0.4 mW mm$^{-2}$ with 6 h pulsed protocol consisting of 400 ms on/4000 ms off cycles). CD concentration: 10 μg ml$^{-1}$. Fluorescence values are normalized over CTRL DARK at 24 h and averaged over 3 biological replicates. All data are represented as mean ± SEM.

 

with 400 ms on and 4000 ms off cycles. Results in Fig. 4(b) show no statistically significant variation between the proliferation ability of CD-treated cell cultures and untreated controls, whether in the dark or after light photostimulation. In all cases, HEK-293 cells show exponential growth in proliferation, as expected in the absence of toxic compounds and/or phototoxic damage.

To investigate the possibility of modulating cell physiological activity upon CD photoexcitation, we study $Ca^{2+}$ ion dynamics (Fig. 5). $Ca^{2+}$ molecule is known as a universal messenger, since intra/extracellular $Ca^{2+}$ ion fluxes regulate cell homeostasis and cell signal transduction, virtually controlling all physiological processes in cells,[73,74] including neurotransmitter release, gene expression, cell cycle, proliferation and migration, contraction, metabolism, just to cite some.[75] Importantly, an increase in intracellular $Ca^{2+}$ concentration can operate over a very wide dynamic range, from microseconds up to a few hours; moreover, the spatial location of the $Ca^{2+}$ sources further increases the versatility and multitude of cellular pathways involved in $Ca^{2+}$ ion regulation. Thus, the opportunity to precisely modulate $Ca^{2+}$ signaling at the sub-cellular level in a reversible, non-invasive manner raises broad interest in the fundamental study of cellular physiology and as a promising therapeutic target.[76] The pharmacological approach is accepted as a golden standard, but it often lacks selectivity, reversibility and spatial resolution. The use of light may in principle circumvent these limitations, and several optically responsive functional nanomaterials have been successfully employed for $Ca^{2+}$ modulation. Examples include silicon nanowires,[77,78] gold nanorods,[79] copper sulfide,[80] polymer nanoparticles and pigments,[53,81,82] organic molecules,[83,84] and carbon nanohorns.[47] Inorganic nanomaterials are usually very efficient and exhibit excellent photoelectrochemical stability, but they often suffer from poor biocompatibility. Conversely, organic compounds are very well tolerated, even in *in vivo* chronic conditions, but at the cost of limited photostability and efficiency. In this context, it is worth asking whether CDs may represent an ideal compromise for reliable and safe optical modulation of intracellular $Ca^{2+}$ signaling.

$Ca^{2+}$ ion transients were measured by employing a $Ca^{2+}$ sensitive fluorophore, Fluo-4, which, upon selective binding with intracellular $Ca^{2+}$ ions, becomes fluorescent. Thus, Fluo-4 fluorescence variation changes are directly proportional to intracellular $Ca^{2+}$ ion concentration variations. In this experiment $Ca^{2+}$ probe excitation and CD photostimulation are

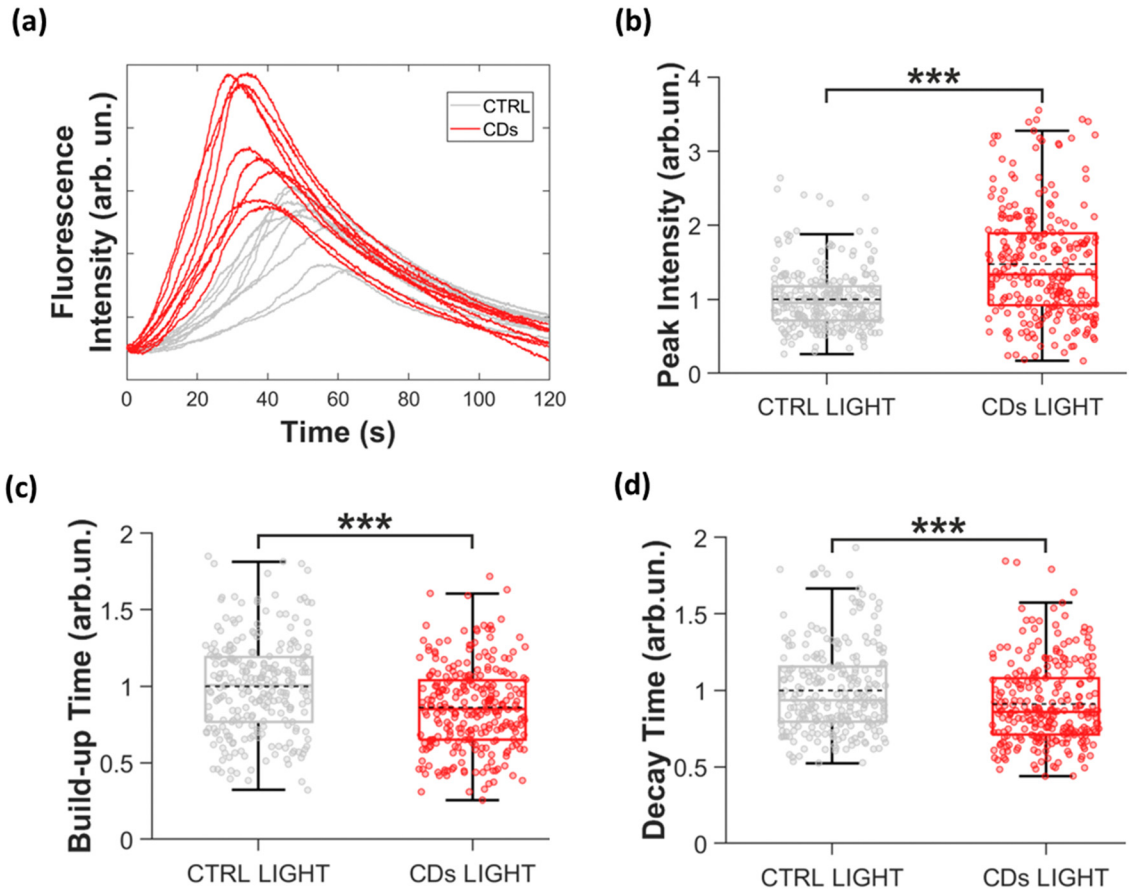


Fig. 5 (a) Representative curves of $Ca^{2+}$ transients in CD-treated and control cell cultures (red and grey lines, respectively); (b)–(d) peak amplitude, build up time and decay time extracted from $Ca^{2+}$ ion time traces. Fluo-4 and CDs are simultaneously excited, by using a broad LED excitation spectrum peaking at 474 ± 50 nm, a CW photoexcitation density of 26 mW $mm^{-2}$, and a total duration of 3 minutes. *N* samples: $N = 16$ (CDs light), $N = 15$ (CTRL light). *n* cells: $n = 265$ (CDs light), $n = 254$ (CTRL light). Mann Whitney (b), (d) and Student's (c) *t*-test statistical test, *P*-values: *** for $p < 0.001$.

carried out simultaneously, by using the same photoexcitation protocol (see Experimental section for technical details). Representative fluorescence images of CD-treated and untreated HEK-293 cell cultures are shown in the ESI,† Fig. S7. Fluorescence variation is evaluated over Regions of Interest covering single cell areas, and the values reported in the following represent the average over multiple cells ($n$ = 265 cells for CDs, $n$ = 254 cells for CTRL light), acquired from 3 independent biological replicates. Fig. 5(a) shows representative time traces of intracellular $Ca^{2+}$ ion concentration changes recorded in CD-treated (red) and untreated (grey) cells. Temporal behavior is in line with existing reports for HEK-293 cells.[53] For a quantitative analysis, we evaluate main features of $Ca^{2+}$ ion dynamics (schematically represented in Fig. S8a, ESI†), namely the peak amplitude (Fig. 5(b)), the full width half maximum (FWHM, Fig. S8b, ESI†), the build-up time, defined as the time interval corresponding to the 10–90% $Ca^{2+}$ signal (Fig. 5(c)), and the decay time, evaluated by fitting the $Ca^{2+}$ signal decay by a single exponential decay curve (Fig. 5(d)). Data were analyzed after normalization to the mean of the control light group, for each of the 3 biological replicates (see the Experimental section for technical details and Table in Fig. S8c, ESI† for average data). The treatment with CDs leads to a significant change in the $Ca^{2+}$ ion trafficking. Specifically, the $Ca^{2+}$ transients in HEK-293 cells treated with CDs exhibit a notable increase in peak $Ca^{2+}$ intensity (+47%, Fig. 5(b)), indicating a higher intracellular $Ca^{2+}$ concentration. The temporal profile is also significantly affected, showing both 14% reduction of the build-up time (Fig. 5(c)), and a 9% decrease of the decay time (Fig. 5(d)). Consequently, the shape of the $Ca^{2+}$ transient curve is modified, and the FWHM is reduced by 6%, compared to the control condition (Fig. S8, ESI†).

In brief, photoexcited CDs significantly affect $Ca^{2+}$ ion trafficking, by increasing absolute intracellular concentration and by shortening the time profile. A more in-depth study would be needed to fully elucidate the physiological origin of the observed phenomenological effect, clarifying whether the observed concentration increase originates from modulation of intracellular $Ca^{2+}$ sources (such as the sarcoendoplasmic reticulum or the mitochondria) or from modulation of $Ca^{2+}$ permeable channels expressed on the cell membrane. As well, the full reversibility of the effect, and the light dose and CD concentration dependence, represent very interesting aspects, which will be the object of the future, dedicated work. Here, we finally focus our attention on the understanding of the photomodulation mechanism.

The functional interplay between $Ca^{2+}$ ion dynamics and ROS concentration has been largely reported as fundamental to the maintenance of intracellular homeostasis.[85–87] In particular, ROS modulation induced by photoelectrochemically active materials upon visible light excitation has been identified as the major transduction mechanism leading to $Ca^{2+}$ modulation.[85,88]

On the other side, N-CDs have been reported to possess excellent oxygen photosensitization performance, showing effective generation of different ROS species, including singlet oxygen $^1O_2$, produced by energy transfer processes, $^{\bullet}O_2^-$, produced by electron transfer, and $H_2O_2$, with a relative efficacy much higher in the first two cases. Very interesting, preliminary applications of N-CDs in photodynamic therapy were reported, by using mammary carcinoma cells as tumor targets and UV-light irradiation (365 nm, 3 mW $cm^{-2}$, CW for 5 minutes) for ROS photoelectrochemical generation.[34]

Therefore, based on the existing literature both on $Ca^{2+}$/ROS interplay and on CDs as oxygen photosensitizers, we verify that

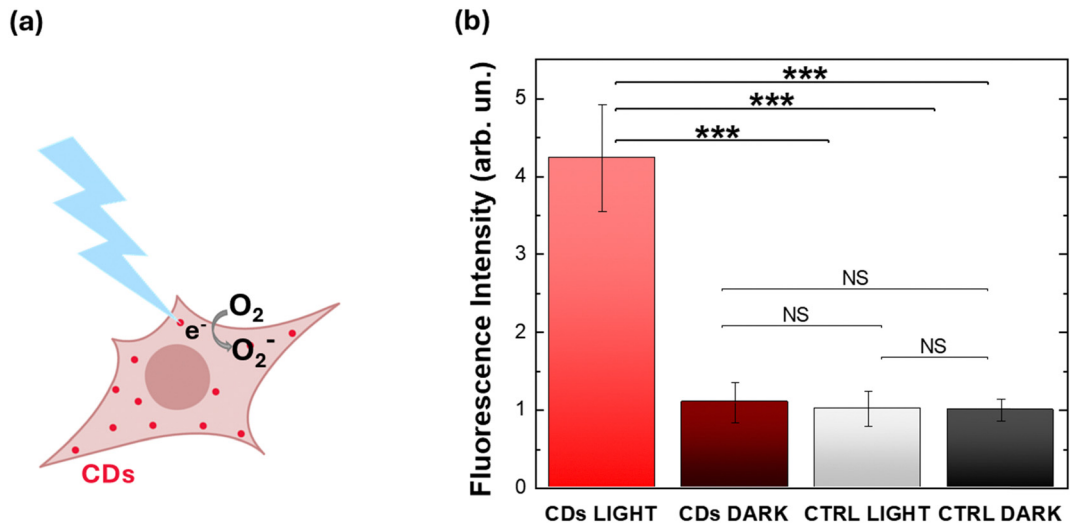


Fig. 6 (a) Sketch representing superoxide generation occurring directly inside the cell cytosol upon CD photostimulation. (b) Intracellular ROS production measured by 10 μM $H_2$DCF-DA fluorescence. The $y$ axis indicates the mean fluorescence intensity of the ROS-sensitive probe internalized within cells. The fluorescence intensity variation is measured in CD-treated cells upon photoexcitation (red), as compared to control sample cohorts (untreated and/or not exposed to photoexcitation). Optical excitation protocol: LED emission spectrum peaking at 474 nm, photoexcitation density 26 mW $mm^{-2}$. Data are represented as mean ± SEM values, over 4 biological replicates. $N$ samples: $N$ = 16 (CDs light), $N$ = 16 (CDs dark), $N$ = 16 (CTRL light), $N$ = 16 (CTRL dark). $n$ cells: $n$ = 480 (CDs light), $n$ = 480 (CDs dark), $n$ = 420 (CTRL light), $n$ = 420 (CTRL dark). $t$-Test, $P$-values: *** for $p < 0.001$; NS = not significant.

 

N-CDs synthesized here can induce an increase in HEK-293 intracellular ROS concentration. We use $H_2$DCF–DA as a ROS probe, and we compare intracellular ROS concentration variation in CD-treated and control samples, either in the dark or upon illumination (Fig. 6). Results unambiguously indicate that only the synergistic action of N-CDs and optical excitation turns into effective modulation of ROS concentration, while ROS levels in control samples (either untreated or in the dark) are not affected. Moreover, the 4-fold relative percentage increase occurs under *eu*stress conditions, carrying no sign of phototoxicity or CD-triggered detrimental impact on cell physiology, as verified by viability assays and $Ca^{2+}$ imaging experiments.

# Conclusions

In this study, we investigated the use of sustainable and biocompatible N-CDs for *in vitro* optical regulation of intracellular redox balance. Compared to other recently employed carbon-based materials for optical, non-invasive modulation of redox states,[43,44,46–49,51–53,85] CDs offer distinct advantages, including enhanced biocompatibility, electrochemical stability, and favorable emission properties which enable precise localization using standard fluorescence microscopy. Nanometric dimensions ($<10$ nm) support efficient internalization without adversely or irreversibly affecting the cell membrane properties.

The N-CDs proposed in this work were synthesized using sustainable methods, starting from abundant, non-cytotoxic materials (citric acid and urea), through a solvothermal process and showed a narrow size distribution centered around 3.25 nm. Nitrogen doping enhanced CD absorption and fluorescence properties, resulting in a broad optical absorption spectrum in the visible range, indicative of effective carbonization and extended conjugation. FT-IR spectroscopy further verified the presence of functional groups, affirming the formation of conjugated aromatic structures that contribute to their favorable electrochemical characteristics.

After investigating the photoelectrochemical activity of CDs in promoting oxygen reduction reactions under visible light excitation, we developed biohybrid interfaces utilizing a non-tumoral cell line. We optimized CD concentration and light excitation protocols to ensure optimal cell internalization while maintaining normal proliferation. We demonstrated that the photoexcitation of internalized CDs results in an increased peak amplitude and acceleration of intracellular $Ca^{2+}$ ion dynamics. Furthermore, we observed a 4-fold increase in intracellular ROS concentration upon visible light excitation of N-CDs, confirming their potential for optically modulating both ROS levels within eustress and $Ca^{2+}$ dynamics. These results pave the way for the optical modulation of intracellular signaling with unmatched spatial resolution, especially when combined with tailored functionalization to selectively target specific cell organelles. In perspective, this capability could help unravel the complex interplay between ROS and $Ca^{2+}$ signaling in the mitochondria and sarcoplasmic reticulum.[73]

Overall, reported findings unveil new possibilities for the application of light-sensitive N-CDs in redox-based modulation of physiological signaling. The synergistic integration of biocompatible nanomaterials with optical stimulation may pave the way for a new 'photoredox' medicine, equipping biologists and clinicians with innovative tools for both fundamental physiological research and therapeutic applications.

# Material and methods

### Carbon dot synthesis and characterization

All reagents were purchased from commercial sources, citric acid from Tokyo Chemical Industry, DMF from Merck and urea from J. T. Baker Chemicals, and used as received without further purification. CDs were synthesized by the solvothermal process in a 20 ml Teflon-lined autoclave. 1.9 g of citric acid and 0.6 g of urea were dissolved in 10 ml of dimethylformamide and transferred to the autoclave. The autoclave was heated at 200 °C for 9 hours. The reaction crude was centrifuged at 1300 rpm for 30 min and then it was precipitated. The supernatant solution was purified through silica gel chromatography using hexane/ethanol 4 : 6 as the eluent.

IR-spectra were recorded with a Spectrum One FTIR spectrometer (PerkinElmer, Waltham, MA, USA) equipped with a deuterated triglycine sulphate (DTGS) detector by drop-casting a water solution of Cds on a Thallium Bromoiodide (KRS-5) window. UV-visible absorption spectra were recorded with a Lambda 900 spectrometer (PerkinElmer, Waltham, MA, USA). PL spectra were obtained with a NanoLog composed of a iH320 spectrograph equipped with a Synapse QExtra charge-coupled device. Excitation was provided by a monochromated 450W Xe lamp. The spectra were corrected for the instrument response. TEM analysis was performed on a JEOL JEM 2200-FS field emission microscope, equipped with in-column Omega filter, operated at 200 kV. For the analysis, the samples were deposited from stock solutions by drop casting over a carbon coated copper grid.

### X-ray photoelectron and nuclear magnetic resonance spectra

XPS has been carried out in a UHV apparatus equipped with a non-monochromatized X-ray source (Mg $K_\alpha$ photon at 1253.6 eV), while photoelectrons have been analyzed through a VSW HA100 hemispherical analyzer with a total energy resolution of 0.86 eV. Core level binding energies (BEs) have been normalized using the C1s $sp^2$ signal at 284.8eV as the reference. A BE shift due to charging phenomena has been found (all core level spectra have been rescaled). Long range spectra have been acquired at a pass energy (PE) of 50 eV, while high resolution core levels have been acquired at a PE of 20 eV. A CD water solution has been deposited on a silicon substrate and dried before the analysis. A silicon substrate analysis has been moreover performed to clearly separate the contribution of CD from the substrate. The $^1$H NMR spectrum was recorded with a Bruker ARX 400 MHz spectrometer (Bruker, Karlsruhe, Germany) in $D_2O$.

### Photoelectrochemistry

Prior to electrochemical measurements, CD-treated ITO electrodes were prepared by drop casting a CD water dispersion

(80 μl of 1 mg $ml^{-1}$ mother solution) onto ITO slabs (2.5 × 0.6 cm), pre-treated with an oxygen plasma asher (Diener Femto PCCE) for 10 minutes. The photoelectrochemical activity of CDs was measured using an electrochemical cell in three-electrode configuration, comprising the ITO/CDs substrate as the working electrode (WE), a KCl-saturated Ag/AgCl wire as the reference electrode (RE), and a platinum wire as the counter electrode (CE). The cell was divided into two compartments, joined by a saline bridge. The RE and CE were placed in one compartment, the WE in the other. Krebs Ringer's (KRH) extracellular solution (5 mM HEPES; 135 mM NaCl, 5.4 mM KCl, 1 mM $MgCl_2$, 1.8 mM $CaCl_2$, 10 mM glucose, all purchased from Sigma Aldrich; pH adjusted to 7.4 with NaOH) was employed as the supporting electrolyte. The measurement was carried out at the open circuit potential, estimated preliminarily (about 160 mV). Light, incident from the ITO side, was provided by a Thorlabs LED (photoexcitation peak at 470 nm, 3 minutes CW illumination, 1.8 mW $mm^{-2}$).

### Cell culture and viability assay

HEK-293 cells were grown in Dulbecco's modified Eagles' medium (D-MEM, Sigma Aldrich) with 10% fetal bovine serum (FBS, Sigma Aldrich), supplemented with 2 mM glutamine (Sigma Aldrich) and 100 U $ml^{-1}$ streptomycin (Sigma Aldrich). The cells were kept in T-75 culture flasks and maintained in an incubator at 37 °C under a humidified atmosphere with 5% $CO_2$. After reaching 80–90% confluence, the cells were detached by incubation with 0.5% trypsin–0.2% EDTA (Sigma Aldrich) for 5 min and then plated for experiments. To promote cell adhesion, a layer of 1 mg $ml^{-1}$ fibronectin (from bovine plasma, Sigma Aldrich) in phosphate buffer saline (PBS, Sigma Aldrich) was deposited on the surface of the glass coverslips and incubated for 30 min. After rinsing fibronectin with PBS, cells were plated on round glass samples at a density of about $8 \times 10^3$ cells per $cm^2$ and cultured in 12 well plates and eventually treated with CDs. For MTT and AlamarBlue assays, HEK cells were seeded at a $7 \times 10^3$ cells $cm^{-2}$ density in 96 well plates and on glass substrates in 12 well plates, respectively. CDs (1 mg $ml^{-1}$ in MilliQ water) were added to the cell culture medium at different concentrations (5, 10, 25, 50, and 200 μg $ml^{-1}$).

Cell proliferation was evaluated at 24, 48, and 168 h after plating, in 3 biological replicates by adding AlamarBlue cell reagent to the cell culture medium at a volume concentration of 1 : 10. The samples were incubated for 3 h at 37 °C, 5% $CO_2$ in the dark. Then, three aliquots of culture media were placed in black 96-well microplates and their fluorescence was acquired using a Tecan Spark microplate reader (excitation wavelength: 530 nm, emission acquired at 590 nm). After each time point, the growth medium was replaced with the fresh medium. In the case of illumination conditions, HEK-293 cell cultures were stimulated in the incubator by using an LED with emission centered at 470 nm for 6 hours (0.4 mW $mm^{-2}$), with a pulsed protocol consisting of 400 ms on/4000 ms off cycles. MTT was performed after 1 and 5 days *in vitro*; for each time point, the culture medium was removed and replaced with the fresh medium supplemented with 1 mg $ml^{-1}$ MTT reagent (previously dissolved in PBS, 5 mg $ml^{-1}$); cells were re-incubated at 37 °C for 3 h. The culture medium was then removed and 200 μL of dimethyl sulfoxide (DMSO, Sigma Aldrich) was added to dissolve formazan crystals. The absorbance of the solution (at 570 nm) was measured with a TECAN Spark microplate reader.

### Confocal imaging

HEK cells were plated on glass slides in 12 well plates at $4 \times 10^3$ cells per well density and were incubated with CDs at a 10 μg $mL^{-1}$concentration for 24 h. The cell membrane and nuclei were stained, respectively, using Cell Mask Green (Thermo Fisher, exc/em wavelength, 522/535 nm) and Hoechst (Thermo Fisher, exc/em, 350/461 nm). Z-Stacks were acquired with an upright microscope (Olympus BW63), equipped with a 60× water immersion objective, a spinning disk confocal module (X-Light V2 spinning disk module from Crest Optics) and a sCMOS Camera (Prime BSI, Teledyne Photometrics; Tucson, Arizona, USA). The system, comprising LED and laser light sources (Spectra III and Celesta, from Lumencor), was assembled by Crisel Instruments. Excitation/emission wavelengths were 530/660 nm for CDs. The experiments were carried out at room temperature. Images were processed using ImageJ.

### Intracellular $Ca^{2+}$ measurements

Cells were seeded on round glass samples in 12-well plates at a $4 \times 10^4$ cells per well density. Samples were incubated for 30 min at 37 °C with a 1.5 μM Fluo-4 (Life Technologies) in KRH extracellular solution. After incubation with Fluo-4, the cells were washed for 15 min with pre-warmed extracellular solution. The cells treated with CDs, as well as CTRL samples, were illuminated for 3 min (emission peak wavelength: 474 nm; photoexcitation density: 26 mW $mm^{-2}$, spot size: 0.9 $mm^2$) by using an LED source light (Lumencor Spectra X light engine). Fluo-4 excitation is simultaneously carried out, by using the same excitation protocol. Videos were recorded with an inverted microscope, Nikon Eclipse Ti, equipped with an Analog-WDM Camera (Cool Snap Myo, Photometrics). Variation in fluorescence intensity was evaluated over Regions of Interest covering single cell areas, and reported values represent the average over multiple cells. Image processing was carried out using ImageJ and subsequently analyzed using Origin 2020. Measurements were repeated in 3 biological replicates, with $n$ = 265 cells for CDs and $n$ = 254 cells for CTRL. Fluorescence intensity transient curves were imported and analyzed using MATLAB R2020b. The peak amplitude was calculated as the difference between the maximum and the minimum Fluo-4 fluorescence intensity values, upon appropriate normalization to the background. Rising time was defined as the time required to reach 90% of peak intensity from 10% peak intensity. Full width at half maximum (FWHM) was determined by subtracting the abscissa values corresponding to 50% of peak intensity. For decay analysis, an exponential decay model, $f(t) = a \cdot \exp(-t/b) + c$ was used to fit the $Ca^{2+}$ transient data. Here, $a$ is the amplitude, $b$ is the decay time, and $c$ is the baseline offset. Initial estimates for $a$ were obtained

 

from fluorescence intensity shortly after the peak, $b$ was initially set to 3, and $c$ was approximated from the last few data points. All data were normalized to the mean of the CTRL light group for the respective biological replicate. Differences between the CTRL light and CD light groups were assessed using Student's $t$-test or the Mann Whitney test for non-normally distributed data. $P$-Values were categorized as follows: *** for $p < 0.001$, ** for $p < 0.01$, and * for $p < 0.05$.

#### Reactive oxygen species (ROS) detection

2′,7′-Dichlorofluorescein diacetate ($H_2$DCF-DA, purchased from Sigma Aldrich) was employed for intracellular detection of ROS. This probe has excitation/emission wavelengths of 488/515 nm. HEK cells were seeded on round glass samples in 12 well plates at a $4 \times 10^4$ cells per well density. CDs dispersed in MilliQ water were administered to cells 3 hours after plating, by diluting them in the cell culture medium up to the desired concentration, corresponding to 10 μg ml$^{-1}$. The measurements were performed 24 hours after plating. Non-internalized CDs were removed by subsequent, repeated rinses of the extracellular medium. One region in each sample (CDs treated cells and control, untreated cells) was photo-excited for 3 min with an LED system (Lumencor Spectra X light engine, objective 20×, emission peak wavelength 474 nm, photoexcitation density 26 mW mm$^{-2}$). Subsequently, cells were incubated with a 10 μM $H_2$DCF–DA probe for 30 minutes at 37 °C. After careful wash-out of the excess probe from the extracellular medium with KRH extracellular solution, the fluorescence of the probe was recorded (objective 20X, emission peak wavelength 474 nm, photoexcitation density 1.5 mW mm$^{-2}$; integration time 50 ms, 100 MHz, binning 1) with an inverted microscope (Nikon Eclipse Ti), equipped with an analog-WDM camera (Cool Snap Myo, Photometrics). Then, the fluorescence of the probe was recorded in a region of the same sample that was not previously exposed to photoexcitation. The variation of fluorescence intensity with respect to the background was evaluated over Regions Of Interest (ROI) covering single cell areas. Reported mean fluorescence values represent the average of fluorescence intensity over multiple cells and different samples. Measurements were repeated in 4 biological replicates (total number of samples: $N$ = 16 (CDs light), $N$ = 16 (CDs dark), $N$ = 16 (CTRL light), and $N$ = 16 (CTRL dark); total number of cells: $n$ = 480 (CDs light), $n$ = 480 (CDs dark), $n$ = 420 (CTRL light), and $n$ = 420 (CTRL dark)). Image processing was carried out using ImageJ and subsequently analyzed using Origin 2020. Data were represented as mean ± SEM. The significance of differences between two groups was evaluated with Student's $t$-test. $P$-Values: *** for $p < 0.001$, ** for $p < 0.01$, * for $p < 0.05$.

## Author contributions

P. Lagonegro synthesized the CDs and carried out optical characterization, with help from F. Turco and B. Squeo. C. Marzuoli carried out cell cultures, viability assays, ROS measurements, $Ca^{2+}$ imaging, with help from C. Bellacanzone. G. Tullii carried out chronoamperometry and fluorescence confocal microscopy. F. Rossi carried out TEM experiments. E. Mancinelli contributed to $Ca^{2+}$ dynamics data analysis and fitting. M. C. Pasini and M. R. Antognazza conceived, conceptualized, supervised and supported the work. All authors contributed to data interpretation and manuscript drafting.

## Data availability

I hereby declare that all data for this article, including the main manuscript and ESI,† will be uploaded and made available in the IIT public repository, at the following link: https://dataverse.iit.it/

## Conflicts of interest

There are no conflicts to declare.

## Acknowledgements

MRA, CM, GT, CB, and EM acknowledge support from the European Research Council (ERC) under the European Union's Horizon 2020 Research and Innovation Program 'LINCE', grant agreement no. 803621. MRA, PL, FT, BS, and MCP acknowledge support from Fondazione Cariplo, under the project Functional Carbon Dots for ENhancing Tomato Production In a Circular Economy (FENICE) scheme, project no. 2021-0626.

## References

1 Y.-P. Sun, B. Zhou, Y. Lin, W. Wang, K. A. S. Fernando, P. Pathak, M. J. Meziani, B. A. Harruff, X. Wang, H. Wang, P. G. Luo, H. Yang, M. E. Kose, B. Chen, L. M. Veca and S.-Y. Xie, *J. Am. Chem. Soc.*, 2006, **128**, 7756–7757.
2 H.-L. Yang, L.-F. Bai, Z.-R. Geng, H. Chen, L.-T. Xu, Y.-C. Xie, D.-J. Wang, H.-W. Gu and X.-M. Wang, *Mater. Today Adv.*, 2023, **18**, 100376.
3 C. Sakdaronnarong, A. Sangjan, S. Boonsith, D. C. Kim and H. S. Shin, *Catalysts*, 2020, **10**, 320.
4 M. P. Aji, A. L. Wati, A. Priyanto, J. Karunawan, B. W. Nuryadin, E. Wibowo, P. Marwoto and S. Sulhadi, *Environ. Nanotechnol., Monit. Manage.*, 2018, **9**, 136–140.
5 D. S. Monje, K. M. Chacon, I. C. Galindo, C. Castaño, L. M. Ballesteros-Rueda, G. C. Valencia, M. C. Gonzalez and D. F. Mercado, *Mater. Today Chem.*, 2021, **20**, 100445.
6 G. Tong, J. Wang, R. Wang, X. Guo, L. He, F. Qiu, G. Wang, B. Zhu, X. Zhu and T. Liu, *J. Mater. Chem. B*, 2014, **3**, 700–706.
7 R. de Boëver, A. Langlois, X. Li and J. P. Claverie, *JACS Au*, 2021, **1**, 843–851.
8 A. Kelarakis, *MRS Energy Sustain.*, 2014, **1**, 2.
9 D. Ozyurt, M. A. Kobaisi, R. K. Hocking and B. Fox, *Carbon Trends*, 2023, **12**, 100276.
10 R. Rauti, M. Musto, S. Bosi, M. Prato and L. Ballerini, *Carbon*, 2019, **143**, 430–446.

11 K. A. S. Fernando, S. Sahu, Y. Liu, W. K. Lewis, E. A. Guliants, A. Jafariyan, P. Wang, C. E. Bunker and Y.-P. Sun, *ACS Appl. Mater. Interfaces*, 2015, **7**, 8363–8376.
12 J. Briscoe, A. Marinovic, M. Sevilla, S. Dunn and M. Titirici, *Angew. Chem., Int. Ed.*, 2015, **54**, 4463–4468.
13 W. Wang, Y.-C. Lu, H. Huang, J.-J. Feng, J.-R. Chen and A.-J. Wang, *Analyst*, 2014, **139**, 1692–1696.
14 Y. Park, J. Yoo, B. Lim, W. Kwon and S.-W. Rhee, *J. Mater. Chem. A*, 2016, **4**, 11582–11603.
15 W. Liu, C. Li, Y. Ren, X. Sun, W. Pan, Y. Li, J. Wang and W. Wang, *J. Mater. Chem. B*, 2016, **4**, 5772–5788.
16 J. Shen, Y. Li, Y. Su, Y. Zhu, H. Jiang, X. Yang and C. Li, *Nanoscale*, 2015, **7**, 2003–2008.
17 R. K. Singh, A. G. Kurian, K. D. Patel, N. Mandakhbayar, N.-H. Lee, J. C. Knowles, J.-H. Lee and H.-W. Kim, *ACS Appl. Bio Mater.*, 2020, **3**, 2218–2229.
18 R. K. Singh, K. D. Patel, C. Mahapatra, M. S. Kang and H.-W. Kim, *ACS Appl. Mater. Interfaces*, 2016, **8**, 24433–24444.
19 K. D. Patel, R. K. Singh and H.-W. Kim, *Mater. Horiz.*, 2019, **6**, 434–469.
20 H. Cai, J. Ma, X. Xu, H. Chu, D. Zhang and J. Li, *J. Mater. Chem. B*, 2020, **8**, 5655–5666.
21 B. Zhi, Y. Cui, S. Wang, B. P. Frank, D. N. Williams, R. P. Brown, E. S. Melby, R. J. Hamers, Z. Rosenzweig, D. H. Fairbrother, G. Orr and C. L. Haynes, *ACS Nano*, 2018, **12**, 5741–5752.
22 S.-T. Yang, L. Cao, P. G. Luo, F. Lu, X. Wang, H. Wang, M. J. Meziani, Y. Liu, G. Qi and Y.-P. Sun, *J. Am. Chem. Soc.*, 2009, **131**, 11308–11309.
23 Y. Zhang, M. Wu, M. Wu, J. Zhu and X. Zhang, *ACS Omega*, 2018, **3**, 9126–9145.
24 N. M. Amal, M. Shiddiq, B. Armynah and D. Tahir, *Luminescence*, 2022, **37**, 2006–2017.
25 M. Sudolská and M. Otyepka, *Appl. Mater. Today*, 2017, **7**, 190–200.
26 S. Sarkar, M. Sudolská, M. Dubecký, C. J. Reckmeier, A. L. Rogach, R. Zbořil and M. Otyepka, *J. Phys. Chem. C*, 2016, **120**, 1303–1308.
27 K. Holá, M. Sudolská, S. Kalytchuk, D. Nachtigallová, A. L. Rogach, M. Otyepka and R. Zbořil, *ACS Nano*, 2017, **11**, 12402–12410.
28 T. Pillar-Little and D. Y. Kim, *RSC Adv.*, 2017, **7**, 48263–48267.
29 Y.-N. Hao, H.-L. Guo, L. Tian and X. Kang, *RSC Adv.*, 2015, **5**, 43750–43755.
30 F. A. Permatasari, R. Umami, C. D. D. Sundari, T. R. Mayangsari, A. L. Ivansyah, F. Muttaqien, T. Ogi and F. Iskandar, *Nano Res.*, 2023, **16**, 6001–6009.
31 K. G. Nguyen, I.-A. Baragau, R. Gromicova, A. Nicolaev, S. A. J. Thomson, A. Rennie, N. P. Power, M. T. Sajjad and S. Kellici, *Sci. Rep.*, 2022, **12**, 13806.
32 P. Lagonegro, U. Giovanella and M. Pasini, *Coatings*, 2021, **11**, 5.
33 B. Ardini, C. Manzoni, B. Squeo, F. Villafiorita-Monteleone, P. Grassi, M. Pasini, M. Bollani and T. Virgili, *Coatings*, 2023, **13**, 785.
34 S. Wu, R. Zhou, H. Chen, J. Zhang and P. Wu, *Nanoscale*, 2020, **12**, 5543–5553.
35 H. Qi, L. Qiu, X. Zhang, T. Yi, J. Jing, R. Sami, S. F. Alanazi, Z. Alqahtani, M. D. Aljabri and M. M. Rahman, *RSC Adv.*, 2023, **13**, 2663–2671.
36 X.-L. Guo, Z.-Y. Ding, S.-M. Deng, C.-C. Wen, X.-C. Shen, B.-P. Jiang and H. Liang, *Carbon*, 2018, **134**, 519–530.
37 H. Sies, in *Oxidative Stress*, ed. H. Sies, Academic Press, 2020, pp. 3–12.
38 B. Chance, H. Sies and A. Boveris, *Physiol. Rev.*, 1979, **59**, 527–605.
39 H. Sies, *Redox Biol.*, 2017, **11**, 613–619.
40 H. Sies, C. Berndt and D. P. Jones, *Annu. Rev. Biochem.*, 2017, **86**, 715–748.
41 H. Sies and D. P. Jones, *Nat. Rev. Mol. Cell Biol.*, 2020, **21**, 363–383.
42 O. S. Abdullaeva, I. Sahalianov, M. Silverå Ejneby, M. Jakešová, I. Zozoulenko, S. I. Liin and E. D. Głowacki, *Adv. Sci.*, 2022, **9**, 2103132.
43 L. Bondi, C. Marzuoli, E. Gutiérrez-Fernández, G. Tullii, J. Martín, B. Fraboni, D. Mecerreyes, M. R. Antognazza and T. Cramer, *Adv. Electrode Mater.*, 2023, **9**, 2300146.
44 M. Criado-Gonzalez, L. Bondi, C. Marzuoli, E. Gutierrez-Fernandez, G. Tullii, C. Ronchi, E. Gabirondo, H. Sardon, S. Rapino, M. Malferrari, T. Cramer, M. R. Antognazza and D. Mecerreyes, *ACS Appl. Mater. Interfaces*, 2023, **15**, 35973–35985.
45 A. Savva, A. Hama, G. Herrera-López, T. Schmidt, L. Migliaccio, N. Steiner, M. Kawan, H. Fiumelli, P. J. Magistretti, I. McCulloch, D. Baran, N. Gasparini, R. Schindl, E. D. Głowacki and S. Inal, *Adv. Sci.*, 2023, 2300473.
46 M. Malferrari, G. Tullii, C. Ronchi, C. Marzuoli, I. A. Aziz, M. R. Antognazza and S. Rapino, *Electrochim. Acta*, 2023, **457**, 142429.
47 E. Miyako, J. Russier, M. Mauro, C. Cebrian, H. Yawo, C. Ménard-Moyon, J. A. Hutchison, M. Yudasaka, S. Iijima, L. De Cola and A. Bianco, *Angew. Chem., Int. Ed.*, 2014, **53**, 13121–13125.
48 O. Akhavan and E. Ghaderi, *Nanoscale*, 2013, **5**, 10316–10326.
49 Z. Yan, K. Li, D. Shao, Q. Shen, Y. Ding, S. Huang, Y. Xie and X. Zheng, *RSC Adv.*, 2022, **12**, 8878–8888.
50 R. Fabbri, A. Scidà, E. Saracino, G. Conte, A. Kovtun, A. Candini, D. Kirdajova, D. Spennato, V. Marchetti, C. Lazzarini, A. Konstantoulaki, P. Dambruoso, M. Caprini, M. Muccini, M. Ursino, M. Anderova, E. Treossi, R. Zamboni, V. Palermo and V. Benfenati, *Nat. Nanotechnol.*, 2024, 1–10.
51 G. Tullii, E. Gutierrez-Fernandez, C. Ronchi, C. Bellacanzone, L. Bondi, M. Criado-Gonzalez, P. Lagonegro, F. Moccia, T. Cramer, D. Mecerreyes, J. Martín and M. R. Antognazza, *Nanoscale*, 2023, **15**, 18716–18726.
52 M. Criado-Gonzalez, C. Marzuoli, L. Bondi, E. Gutierrez-Fernandez, G. Tullii, P. Lagonegro, O. Sanz, T. Cramer, M. R. Antognazza and D. Mecerreyes, *Nano Lett.*, 2024, **24**, 7244–7251.

 

53 C. Bossio, I. Abdel Aziz, G. Tullii, E. Zucchetti, D. Debellis, M. Zangoli, F. Di Maria, G. Lanzani and M. R. Antognazza, *Front. Bioeng. Biotechnol.*, 2018, **6**, 114.
54 F. Arcudi, L. Đorđević and M. Prato, *Angew. Chem., Int. Ed.*, 2016, **55**, 2107–2112.
55 X. Miao, D. Qu, D. Yang, B. Nie, Y. Zhao, H. Fan and Z. Sun, *Adv. Mater.*, 2018, **30**, 1704740.
56 X. Zhang, C. Chen, D. Peng, Y. Zhou, J. Zhuang, X. Zhang, B. Lei, Y. Liu and C. Hu, *J. Mater. Chem. C*, 2020, **8**, 11563–11571.
57 C.-L. Shen, Q. Lou, G.-S. Zheng, M.-Y. Wu, J.-H. Zang, K.-K. Liu, L. Dong and C.-X. Shan, *ACS Sustainable Chem. Eng.*, 2022, **10**, 1624–1632.
58 D. Chen, W. Wu, Y. Yuan, Y. Zhou, Z. Wan and P. Huang, *J. Mater. Chem. C*, 2016, **4**, 9027–9035.
59 S. Jing, Y. Zhao, R.-C. Sun, L. Zhong and X. Peng, *ACS Sustainable Chem. Eng.*, 2019, **7**, 7833–7843.
60 S. Tajik, Z. Dourandish, K. Zhang, H. Beitollahi, Q. V. Le, H. W. Jang and M. Shokouhimehr, *RSC Adv.*, 2020, **10**, 15406–15429.
61 H. Wang, C. Sun, X. Chen, Y. Zhang, V. L. Colvin, Q. Rice, J. Seo, S. Feng, S. Wang and W. W. Yu, *Nanoscale*, 2017, **9**, 1909–1915.
62 J. Manioudakis, F. Victoria, C. A. Thompson, L. Brown, M. Movsum, R. Lucifero and R. Naccache, *J. Mater. Chem. C*, 2019, **7**, 853–862.
63 H. Wang, Q. Wang, Q. Wang, W. Dong, Y. Liu, Q. Hu, X. Song, S. Shuang, C. Dong and X. Gong, *J. Cleaner Prod.*, 2023, **411**, 137337.
64 T. Zhang, J. Qu, Y. Yao, Y. Zhang, Y. Ma, D. Wu, Y. Cao, M. Yang, Y. Zhang, M. Tang and Y. Pu, *Chemosphere*, 2020, **251**, 126440.
65 L. Sun, Y. Luo, M. Li, G. Hu, Y. Xu, T. Tang, J. Wen, X. Li and L. Wang, *J. Colloid Interface Sci.*, 2017, **508**, 154–158.
66 C. Xia, J. Feng, C. Ma, H. Xi, N. Song, H. Dong, L. Yu and L. Dong, *Mol. Catal.*, 2023, **535**, 112880.
67 H. Wang, M. Zhang, K. Wei, Y. Zhao, H. Nie, Y. Ma, Y. Zhou, H. Huang, Y. Liu, M. Shao and Z. Kang, *Carbon*, 2021, **179**, 692–700.
68 S. Cailotto, R. Mazzaro, F. Enrichi, A. Vomiero, M. Selva, E. Cattaruzza, D. Cristofori, E. Amadio and A. Perosa, *ACS Appl. Mater. Interfaces*, 2018, **10**, 40560–40567.
69 Q. Li, X. Shen and D. Xing, *Dyes Pigm.*, 2023, **208**, 110784.
70 E. Mosconi, P. Salvatori, M. I. Saba, A. Mattoni, S. Bellani, F. Bruni, B. Santiago Gonzalez, M. R. Antognazza, S. Brovelli, G. Lanzani, H. Li, J.-L. Brédas and F. De Angelis, *ACS Energy Lett.*, 2016, **1**, 454–463.
71 I. Abdel Aziz, L. Maver, C. Giannasi, S. Niada, A. T. Brini and M. R. Antognazza, *J. Mater. Chem. C*, 2022, **10**, 9823–9833.
72 F. Lodola, V. Rosti, G. Tullii, A. Desii, L. Tapella, P. Catarsi, D. Lim, F. Moccia and M. R. Antognazza, *Sci. Adv.*, 2019, **5**, eaav4620.
73 F. Moccia, A. Fiorio Pla, D. Lim, F. Lodola and A. Gerbino, *Front. Physiol.*, 2023, **14**, 1210085.
74 M. J. Berridge, M. D. Bootman and H. L. Roderick, *Nat. Rev. Mol. Cell Biol.*, 2003, **4**, 517–529.
75 D. E. Clapham, *Cell*, 1995, **80**, 259–268.
76 I. A. Aziz and M. R. Antognazza, *MRS Adv.*, 2020, **5**, 3473–3489.
77 R. Parameswaran, K. Koehler, M. Y. Rotenberg, M. J. Burke, J. Kim, K.-Y. Jeong, B. Hissa, M. D. Paul, K. Moreno, N. Sarma, T. Hayes, E. Sudzilovsky, H.-G. Park and B. Tian, *Proc. Natl. Acad. Sci. U. S. A.*, 2019, **116**, 413–421.
78 M. Y. Rotenberg, B. Elbaz, V. Nair, E. N. Schaumann, N. Yamamoto, N. Sarma, L. Matino, F. Santoro and B. Tian, *Nano Lett.*, 2020, **20**, 1226–1232.
79 S. P. Sanchez-Rodriguez, J. P. Sauer, S. A. Stanley, X. Qian, A. Gottesdiener, J. M. Friedman and J. S. Dordick, *Biotechnol. Bioeng.*, 2016, **113**, 2228–2240.
80 W. Gao, Y. Sun, M. Cai, Y. Zhao, W. Cao, Z. Liu, G. Cui and B. Tang, *Nat. Commun.*, 2018, **9**, 231.
81 J.-G. Wu, J.-H. Chen, K.-T. Liu and S.-C. Luo, *ACS Appl. Mater. Interfaces*, 2019, **11**, 21294–21307.
82 D. Rand, M. Jakešová, G. Lubin, I. Vėbraitė, M. David-Pur, V. Derek, T. Cramer, N. S. Sariciftci, Y. Hanein and E. D. Głowacki, *Adv. Mater.*, 2018, 1707292.
83 G. Cabré, A. Garrido-Charles, M. Moreno, M. Bosch, M. Porta-de-la-Riva, M. Krieg, M. Gascón-Moya, N. Camarero, R. Gelabert, J. M. Lluch, F. Busqué, J. Hernando, P. Gorostiza and R. Alibés, *Nat. Commun.*, 2019, **10**, 907.
84 T. Fehrentz, F. M. E. Huber, N. Hartrampf, T. Bruegmann, J. A. Frank, N. H. F. Fine, D. Malan, J. G. Danzl, D. B. Tikhonov, M. Sumser, P. Sasse, D. J. Hodson, B. S. Zhorov, N. Klöcker and D. Trauner, *Nat. Chem. Biol.*, 2018, **14**, 764–767.
85 S. Negri, P. Faris, G. Tullii, M. Vismara, A. F. Pellegata, F. Lodola, G. Guidetti, V. Rosti, M. R. Antognazza and F. Moccia, *Cell Calcium*, 2022, **101**, 102502.
86 S. Negri, P. Faris and F. Moccia, *Int. J. Mol. Sci.*, 2021, **22**, 9821.
87 A. Görlach, K. Bertram, S. Hudecova and O. Krizanova, *Redox Biol.*, 2015, **6**, 260–271.
88 C. Ronchi, C. Galli, G. Tullii, C. Marzuoli, M. Mazzola, M. Malferrari, S. Crasto, S. Rapino, E. Di Pasquale and M. R. Antognazza, *Adv. Sci.*, 2023, 2304303.